ChemComm

COMMUNICATION

View Article Online
View Journal

Cite this: DOI: 10.1039/d3cc01086d

Received 4th March 2023,
Accepted 18th April 2023

DOI: 10.1039/d3cc01086d

rsc.li/chemcomm

In situ $BaSO_4$ coating enabled activation-free and ultra-stable δ-MnO_2 for aqueous Zn-ion batteries†

Lele Liu,[a] Shouxiang Ding,[a] Lu Yao,[a] Mingqiang Liu,[b] Shunning Li,[a] Qinghe Zhao,*[a] Runzhi Qin*[a] and Feng Pan*[a]

***In situ* $BaSO_4$ coating, generated in the first discharging of Ba^{2+} pre-intercalated δ-MnO_2, shortens the activation process by inducing fast proton intercalation and stabilizes the MnO_2 crystal by suppressing Mn dissolution. The cathode delivers a decent electrochemical performance of 210 mA h g^{-1} at 1C with a 98% retention after 200 cycles.**

Rechargeable aqueous Zn-ion batteries (ZIBs) are receiving increasing attention owing to their unique advantages of low price, high safety, and high capacity.[1] Among various cathode materials, MnO_2, with a high theoretical capacity of 308 mA h g^{-1}, high operating voltage of 1.3–1.5 V, and environmental friendliness, is widely studied.[2] A variety of polymorphs have been reported in ZIBs, such as α-MnO_2,[3] β-MnO_2,[4] δ-MnO_2,[5] *etc.* because the tunnel- or layer-type structures are favourable for the insertion/extraction of charge carriers. However, MnO_2 cathodes are still not capable of commercialization, which mainly lies in their shortcomings of unsatisfactory structural stability, as well as the very complicated reaction mechanism in aqueous media.[6] Generally, MnO_2 polymorphs own low initial capacity and suffer from an interminable capacity climbing process, which is the so-called activation process.[7] Besides, the poor structural stability enables easy phase transition, which further results in capacity fading afterwards.[8] Several theories have been put forward trying to explain the mysteries, such as phase evolution,[9] new reaction of dissolution/deposition,[10] *etc.* But the controversy still remains.

Strategies are developed to tackle these issues. For example, the pre-intercalation of various ions and molecules has been widely studied.[11] It is believed that these species can extend the interlayer spacing, thus facilitating the diffusion of charge carriers.[12] Recently, the importance of the material surface is highly valued. Our team has proved that the bulk instability of oxides is actually originated from the surface breakage.[13] The approaches of the majority of surface protections, however, can hardly be applied in MnO_2 cathodes due to their low suitability. Some carbon-based materials are reported to decorate the surface of MnO_2 for conductivity improvement.[14] But these *ex situ* prepared coatings are not capable of completely protecting the crystal.

Herein, taking the layered δ-MnO_2 as a model, we use the pre-intercalation of Ba^{2+} to modify the cathode surface. The $BaSO_4$ layer is *in situ* generated during cycling, which efficiently accelerates the activation process and stabilizes the crystal structure. The cathode presents a remarkable cycling performance of 210 mA h g^{-1} at 1C with no obvious capacity fading after 200 cycles, and 110 mA h g^{-1} at 4C with over 60% capacity retention after 2000 cycles.

The δ-MnO_2 samples are synthesized by a microwave-assisted hydrothermal method, which is stated in detail in the ESI.† While using $KMnO_4$ as the oxidant, K^+ will be inevitably pre-intercalated into the interlayer of δ-MnO_2 to form KMO material.[3,4] Then, the sample with an additional introduction of Ba^{2+} precursor is denoted as BMO for comparison. The structure of the samples is characterized by X-ray diffraction (XRD). As shown in Fig. 1a, both BMO and KMO present diffraction peaks at ~12.1°, 25.6°, 37.0°, 41.1°, and 65.5°, which can be well indexed to the layered phase of MnO_2 (PDF #42-1317, space group of $C2/m$). Note that the diffraction peak of the (001) plane in BMO is slightly lower than that of KMO, indicating an enlarged layer spacing due to the introduction of Ba^{2+}. The detailed elemental composition of Ba, O, and Mn is investigated through X-ray photoelectron spectroscopy (XPS), as shown in Fig. 1b–d. The peaks at 92.3 eV, 780.8 eV, and 796 eV are attributed to $4d_{3/2}$, $3d_{1/2}$, and $3d_{3/2}$ of Ba elements, respectively, which further confirms the intercalation of Ba^{2+} ions in BMO. The O 1s XPS spectra of KMO and BMO can be resolved into three sub-peaks of Mn–O–Mn, Mn–O–H, and H–O–H (Fig. 1c), which are indexed to [MnO_6] octahedrons of the crystal structure, the adsorbed H^+ between layers, and the adsorbed water/crystal water, respectively.[15] In addition, both BMO and

[a] *School of Advanced Materials, Peking University Shenzhen Graduate School, Shenzhen 518055, P. R. China. E-mail: zhaoqh@pku.edu.cn, bushihaoren@pku.edu.cn, panfeng@pkusz.edu.cn*

[b] *Electrochemical Innovation Lab, University College London, London WC1E 7JE, UK*

† Electronic supplementary information (ESI) available. See DOI: https://doi.org/10.1039/d3cc01086d

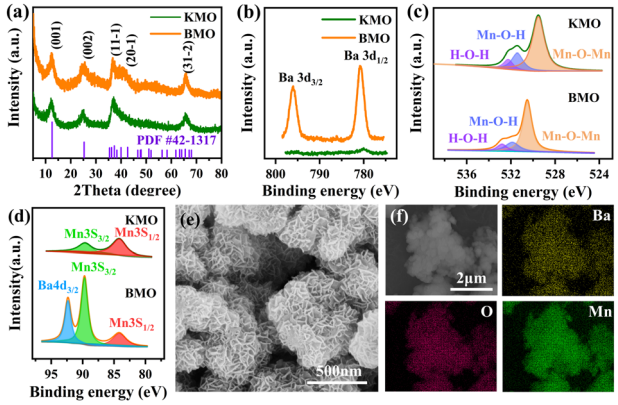

Fig. 1 (a) XRD patterns of BMO and KMO; XPS results of (b) Ba 3d, (c) O 1s, and (d) Mn 3s; (e) SEM image and (f) EDS mapping of BMO.

KMO present nanoflake-like structure (Fig. 1e and Fig. S1, ESI†). The energy dispersive spectrometer (EDS) mapping proves the uniform distribution of Ba, Mn, and O elements in BMO (Fig. 1f), as well as the element distribution in the KMO sample (Fig. S1, ESI†). All of the above-mentioned results prove that Ba^{2+} is successfully introduced as the pillar into the space layer of the δ-MnO_2. The chemical formulae of BMO and KMO are then calculated as $Ba_{0.35}MnO_2{\cdot}0.39H_2O$ and $K_{0.14}MnO_2{\cdot}0.35H_2O$, respectively, which are obtained by thermogravimetric analysis (TGA) and inductively coupled plasma optical emission spectroscopy (ICP-OES) results (Fig. S2 and Table S1, ESI†).

Coin-type cells are assembled to investigate the influence of Ba^{2+} pre-intercalation, and the electrochemical properties of KMO and BMO are compared in Fig. 2. The cyclic voltammetry (CV) plots of BMO with a scan rate of 0.1 mV s^{-1} show a reduction peak at 1.27 V and an oxidation peak at 1.58 V in the first cycle. Then two reduction peaks at 1.40 V and 1.27 V and an oxidation peak at 1.59 V occur in the second cycle. The CV curves of KMO show similar profiles but lower current densities, which indicates inferior electrochemical activity. In addition, the oxidation peaks of KMO are split in the following cycles, which may be attributed to the surface-dominated activation process (Fig. S3, ESI†).

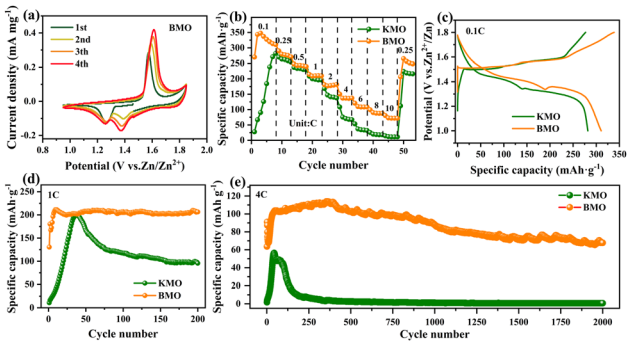

Fig. 2 (a) CV curves of BMO at a scan rate of 0.1 mV s^{-1}; (b) rate performance of BMO and KMO; (c) galvanostatic discharge–charge curves at the 8th cycle of 0.1C; long cycling performance of BMO and KMO at the rate of (d) 1C and (e) 4C.

The rate performance of the two samples is shown in Fig. 2b and Table S2 (ESI†), and the corresponding galvanostatic discharge–charge curves at 0.1C are shown in Fig. S4 (ESI†). Surprisingly, BMO releases a high initial capacity of 270 mA h g^{-1}, presenting an activation-free behaviour. On the contrary, KMO shows a much slower electrochemical activation process in the initial 8 cycles with an initial capacity of only 28 mA h g^{-1}. The phenomenon of low initial capacity and interminable activation of traditional MnO_2 has long been confusing to researchers. Since the fresh MnO_2 is the Zn-poor phase, it is supposed to release full capacity immediately at the very first discharge. Moreover, in the following cycles, BMO delivers a high discharge capacity of 348 mA h g^{-1} in the second cycle, which corresponds to a 24% increase to the maximum capacity of KMO. As the current density increases to higher rates, the capacity of KMO fades rapidly, while BMO continues to deliver significantly better capacity. Fig. 2c provides the galvanostatic discharge–charge profiles of the two samples at the 8th cycle of 0.1C. Apparently, BMO demonstrates higher voltages at each discharging plateau, standing for smaller polarization and facilitated reaction kinetics.

The long cycling tests are performed in order to inspect the structural stability. At the rate of 1C, the capacity of BMO climbs to 210 mA h g^{-1} within 10 cycles, and then keeps no obvious capacity fading for the following 200 cycles (Fig. 2d). In contrast, KMO needs 4 times longer for activation until the capacity reaches 210 mA h g^{-1}, then suffers rapid capacity attenuation. After 200 cycles, BMO offers double capacity than KMO. Note that the GDC profiles in Fig. S5 (ESI†) clearly reveal that the activation process is associated with the proton's behavior, for the capacity contribution of H^+ significantly increases from 25% (1st cycle, 2.7 mA h g^{-1}) to 62% (40th cycle, 123 mA h g^{-1}) in the KMO sample. The performance difference is even broadened at the rate of 4C. KMO shows nearly electrochemical inertness at the outset. Rigmarole activation of 60 cycles is needed until the capacity reaches only 56 mA h g^{-1}. After decaying in the subsequent 190 cycles, KMO loses its electrochemical activity, only releasing 7 mA h g^{-1}. In sharp contrast, BMO discharges an initial capacity of 64 mA h g^{-1} and reaches the capacity of 104 mA h g^{-1} within 35 cycles (Fig. 2e). It still retains over 60% capacity after 2000 cycles, elucidating the superior structure stability enabled by the pre-intercalated Ba^{2+} ions.

Ex situ XRD taken from each charging and discharging state of the initial two cycles is employed to distinguish BMO and KMO samples. Note that after being coated onto the current collector, both the two MnO_2 samples show poor crystallinity and lose the characteristic signals in the XRD patterns. For BMO, nevertheless, a strong signal of $Zn_4SO_4(OH)_6{\cdot}4H_2O$ (PDF 44-0673, denoted as ZHS) emerges at 1.34 V in the first discharge progress (point *B* in Fig. 3a and b). The ZHS owns ultra-low K_{sp} of only 9.8×10^{-34}, and thus it can be regarded as an indicator of local alkalization, or the consumption of protons in other words.[16] The ZHS survives in the first full discharging state of point *C* and vanishes in the following charging process (point *E* and *F*), as well as the earlier stage of the second discharging state (point *G*). Then the ZHS periodically occurs in the discharging process and disappears in charging

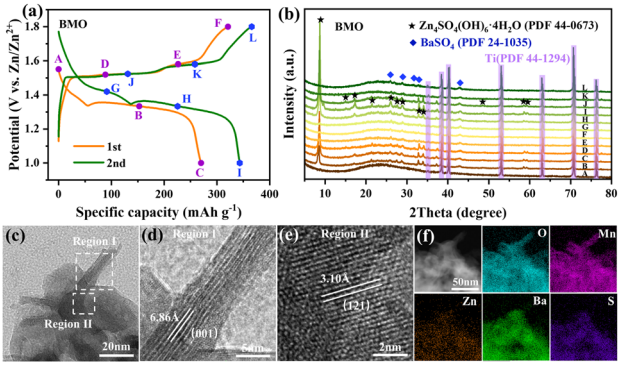

Fig. 3 (a) Galvanostatic discharge–charge curves of BMO at 0.1C; (b) corresponding *ex situ* XRD patterns of different states; (c–e) TEM images of BMO at first discharging state after acid washing; (f) EDS-mapping of O, Mn, Zn, Ba, and S.

process, which is consistent with the well-recognized theory of proton intercalation/deintercalation.[17] In sharp contrast, the signal of ZHS in the KMO sample is not pronounced (Fig. S6, ESI†), and it only occurs at a low cut-off voltage (point *C* and *I* in Fig. S6, ESI†). This means that a very limited amount of protons take part in the reaction, which might be the key point behind the issue of the low initial capacity.

The corresponding SEM images provide more evidence. As shown in Fig. S7 (ESI†), the surface morphology of BMO undergoes periodical evolution. ZHS nanosheets with a diameter of hundreds of nanometers uniformly grow from the very beginning of the first discharging process (point *B* to point *C*). After the subsequent charging, the surface of BMO is covered by mossy-like products. In comparison, lots of craters occur at the KMO surface in the initial discharging (point *B*, Fig. S8, ESI†), and huge ZHS flakes lie on the electrode randomly and sparsely. The KMO electrode then cracks in the full charging process, losing its integrity (point *F*, Fig. S8, ESI†).

Apparently, the only explanation for the difference between the two samples is the pre-intercalated Ba^{2+} in BMO, which is in turn detected as $BaSO_4$ (PDF 24-1035, denoted as BSO) from the first discharging voltage of 1.34 V (line *B* in Fig. 3b). After thorough treatment with the acetic acid solution, the electrode shows no signal of ZHS. However, the diffraction peaks of BSO can still be observed, accounting for strong chemical adhesion between BSO and the substrate (Fig. S9 and S10, ESI†). Transmission electron microscopy (TEM) has been conducted to clarify the formation of BSO. As shown in Fig. 3c, the flaky structures (region I in Fig. 3d) and blocky structures (region II in Fig. 3e) merge with each other. The former, with the crystal spacing of 6.86 Å, is associated with the (001) crystal plane spacing in layered MnO_2; while the latter possessing a lattice fringe spacing of 3.10 Å is indexed to the (121) crystal plane of $BaSO_4$. The corresponding EDS results confirm the uniform distribution of Mn, O, Ba, S, and Zn elements in the cathode (Fig. 3f). Seldom could the two structures be separated, indicating the very tough cohesion. A reasonable deduction can be drawn that Ba^{2+} dissolves along with the intercalation of the charge carriers, and then immediately precipitates with SO_4^{2-} due to the low K_{sp} of BSO (1.1×10^{-10}) and covers the MnO_2 surface. In this way, the BSO works as the coating layer of the cathode. Such coating remains nearly unchanged during the subsequent discharging/charging process (Fig. 3b and Fig. S9, ESI†), further validating its stable structure.

Combining all of the above results, we conclude that the surface reconstruction, *i.e.*, the *in situ* BSO coating, can lead to additional proton intercalation, which is the main reason for the activation-free behavior of BMO. Unlike other ions, the proton is not previously added to the electrolyte. It has to experience two steps to act as a charge carrier: generation from water dissociation, and intercalation, while ZHS is necessary to balance the local pH. Ordinary KMO does not offer proper nucleation sites for ZHS, and thus ZHS is loosely attached to the electrode surface and suffers sluggish growth. According to the chemical equilibrium, less and slower ZHS formation leads to the accumulation of OH^-, thus being unfavorable to the proton release of water and the following proton storage of the cathode. Once BSO is *in situ* generated, however, it exposes numerous [SO_4] tetrahedrons as the nucleation sites due to the inevitable breakage of lattice symmetry at the BSO/electrolyte interface, significantly boosting the precipitation of ZHS and the subsequent proton intercalation. A convincing experiment is then conducted, in which nanocrystal $BaSO_4$ is *ex situ* prepared (denoted as *ex*-BSO) and added into the KMO cathode. The KMO particles and *ex*-BSO flakes are physically jointed and well distributed in the cathode (Fig. S11, ESI†). Surprisingly, under the same test condition of 1C, the composite KMO/*ex*-BSO cathode presents a similar electrochemical performance to BMO. Its initial capacity is improved to 61 mA h g^{-1}, over twice that for KMO (Fig. S12, ESI†). Moreover, it completes the activation process only within 8 cycles, which is 1/5 shorter than KMO. Such enhanced performance can also be rationalized to the fast generation of ZHS and protons with the aid of *ex*-BSO even in the mechanical mixing state.

More electrochemical tests are conducted in order to explore the mechanism of the enhanced performance of BMO. The electrochemical impedance results of the two cathodes show similar profiles, and no other reaction can be distinguished (Fig. S13, ESI†). Besides, the close value of the charge transfer resistance implies similar kinetics for both cathodes. It seems that the Ba^{2+} in the space layer does not trigger additional electrochemical reactions. Then galvanostatic intermittent titration techniques are used to study the kinetics of the intercalation/deintercalation mechanism. As shown in Fig. S14 (ESI†), it is revealed that BMO and KMO own almost the same ion diffusion coefficient during the whole discharging process. This phenomenon demonstrates the fact that, unlike other pre-intercalated ions,[18] Ba^{2+} does not manipulate the internal diffusion of the charge carriers in the bulk cathode.

Consequently, the excellent capacity retention of BMO must be highly related to the external BSO coating. Fig. 4a presents the structure evolution of the BMO cathode in a long cycling test. After the first discharge, the peak intensity of BSO remains unchanged within 150 cycles. It can be semi quantitatively interpreted that the BSO neither dissolves nor grows, which is essential to the coating profession. Furthermore, ICP-OES is

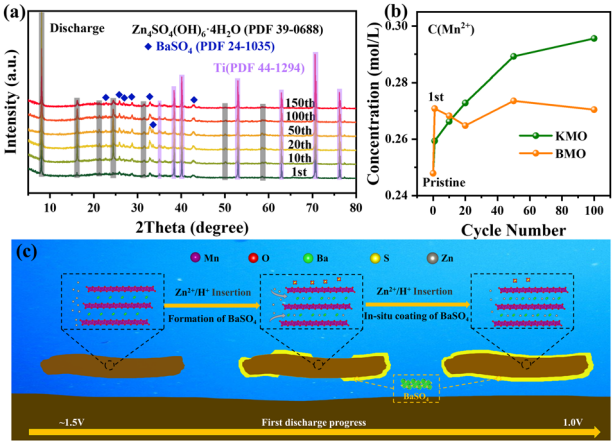

Fig. 4 (a) *Ex situ* XRD patterns of BMO in the long cycling test in full discharging state; (b) corresponding Mn^{2+} concentration in the electrolyte; (c) schematic of the mechanism for $BaSO_4$ coating.

also employed to analyse the electrolyte variation of KMO and BMO at fully discharged states along with cycling. As shown in Fig. 4b, the concentration of Mn^{2+} in the BMO battery increases rapidly after the first discharging, which provides another clue for the formation of BSO. It can be deduced that some Mn^{4+} is reduced to Mn^{3+} after the intercalation of charge carriers, which suffers disproportionation due to the Jahn–Teller effect and releases soluble Mn^{2+} into the electrolyte.[19] Then the very surface of the BMO crystal collapses and Ba^{2+} escapes. The participation of Zn^{2+} as the charge carrier is affirmed by TEM mapping results (Fig. 3f), while the effect of protons is indistinct under the current circumstance. Nevertheless, it does not matter for the phenomenon of Mn dissolution that is widely accepted in the literature,[10,20] as well as our topic of BSO coating. In the following cycles, the concentration of Mn^{2+} remains relatively constant at the level of ~0.27 M, indicating the integrity of the rest of the BMO crystals. Undoubtedly, the tough BSO coating plays a key role in keeping the Mn^{2+} away from the electrolyte, thus improving the integrity of the cathode. The SEM images in Fig. S15 (ESI†) also demonstrate that the BMO cathode remains in its original morphology in both charging and discharging states even after 150 cycles. Accordingly, a schematic describing the effect of the pre-intercalated Ba^{2+} is illustrated in Fig. 4c. As a comparison, the concentration of Mn^{2+} in the KMO battery is incremental in the long cycling test, reaching 0.30 M after 100 cycles. This suggests that the KMO suffers successive Mn^{2+} dissolution without the aid of an *in situ* protection layer, which leads to the loss of active materials and capacity fading.

In summary, a Ba^{2+} pre-intercalated δ-MnO_2 material was synthesized by a microwave-assisted hydrothermal method. With the Mn^{2+} dissolution in the first discharging progress, Ba^{2+} escapes from the lattice and immediately precipitates with SO_4^{2-} from the electrolyte, generating a $BaSO_4$ layer. Such *in situ* coating not only significantly accelerates the electrochemical activation process but also effectively suppresses the further dissolution of Mn^{2+}. Owing to the *in situ* BSO coating, such δ-MnO_2 delivers a decent electrochemical performance of 210 mA h g^{-1} at 1C with a 98% retention after 200 cycles, and 113 mA h g^{-1} at 4C with an over 60% retention within 2000 cycles. This work provides a new idea for surface reconstruction in the activation procedure and a new method of structural stability enhancement *via* surface protection for cathodes in aqueous batteries.

This work was financially supported by the Shenzhen Fundamental Research Program (No. GXWD20201231165807007-20200807111854001), the National Natural Science Foundation of China (52102201), and the Basic and Applied Basic Research Foundation of Guangdong Province (2022A1515110446).

Conflicts of interest

There are no conflicts to declare.

Notes and references

1 X. Wang, Z. Zhang, B. Xi, W. Chen, Y. Jia, J. Feng and S. Xiong, *ACS Nano*, 2021, **15**, 9244–9272.
2 Y. Liang and Y. Yao, *Nat. Rev. Mater.*, 2023, **8**, 109–122.
3 Q. Zhao, A. Song, W. Zhao, R. Qin, S. Ding, X. Chen, Y. Song, L. Yang, H. Lin, S. Li and F. Pan, *Angew. Chem., Int. Ed.*, 2020, **60**, 4169–4174.
4 S. Ding, M. Zhang, R. Qin, J. Fang, H. Ren, H. Yi, L. Liu, W. Zhao, Y. Li, L. Yao, S. Li, Q. Zhao and F. Pan, *Nano-Micro Lett.*, 2021, **13**, 173.
5 Y. Zhao, C. Chang, F. Teng, Y. Zhao, G. Chen, R. Shi, G. I. N. Waterhouse, W. Huang and T. Zhang, *Adv. Energy Mater.*, 2017, **7**, 1700005.
6 W. Z. Dongliang Chao, F. Xie, C. Ye, H. Li, M. Jaroniec and S.-Z. Qiao, *Sci. Adv.*, 2020, **6**, eaba4098.
7 J. Li, N. Luo, L. Kang, F. Zhao, Y. Jiao, T. J. Macdonald, M. Wang, I. P. Parkin, P. R. Shearing, D. J. L. Brett, G. Chai and G. He, *Adv. Energy Mater.*, 2022, **12**, 2201840.
8 C. Li, S. Jin, L. A. Archer and L. F. Nazar, *Joule*, 2022, **6**, 1733–1738.
9 S. Ding, L. Liu, R. Qin, X. Chen, A. Song, J. Li, S. Li, Q. Zhao and F. Pan, *ACS Appl. Mater. Interfaces*, 2021, **13**, 22466–22474.
10 P. Ruan, X. Xu, D. Zheng, X. Chen, X. Yin, S. Liang, X. Wu, W. Shi, X. Cao and J. Zhou, *ChemSusChem*, 2022, **15**, e202201118.
11 X. Chen, P. Ruan, X. Wu, S. Liang and J. Zhou, *Acta Phys.-Chim. Sin.*, 2022, **38**, 2111003.
12 K. Shimokawa, T. Atsumi, N. L. Okamoto, T. Kawaguchi, S. Imashuku, K. Wagatsuma, M. Nakayama, K. Kanamura and T. Ichitsubo, *Adv. Mater.*, 2021, **33**, 2007539.
13 J. Li, C. Lin, M. Weng, Y. Qiu, P. Chen, K. Yang, W. Huang, Y. Hong, J. Li, M. Zhang, C. Dong, W. Zhao, Z. Xu, X. Wang, K. Xu, J. Sun and F. Pan, *Nat. Nanotechnol.*, 2021, **16**, 599–605.
14 J. Xu, X. Hu, M. A. Alam, G. Muhammad, Y. Lv, M. Wang, C. Zhu and W. Xiong, *RSC Adv.*, 2021, **11**, 35280–35286.
15 M. Liu, Q. Zhao, H. Liu, J. Yang, X. Chen, L. Yang, Y. Cui, W. Huang, W. Zhao, A. Song, Y. Wang, S. Ding, Y. Song, G. Qian, H. Chen and F. Pan, *Nano Energy*, 2019, **64**, 103942.
16 J. Zhang, W. Li, J. Wang, X. Pu, G. Zhang, S. Wang, N. Wang and X. Li, *Angew. Chem., Int. Ed.*, 2022, **62**, e202215654.
17 H. Chen, C. Dai, F. Xiao, Q. Yang, S. Cai, M. Xu, H. J. Fan and S. J. Bao, *Adv. Mater.*, 2022, **34**, 2109092.
18 K. Han, F. An, F. Yan, H. Chen, Q. Wan, Y. Liu, P. Li and X. Qu, *J. Mater. Chem. A*, 2021, **9**, 15637–15647.
19 Z. Liu, L. Li, L. Qin, S. Guo, G. Fang, Z. Luo and S. Liang, *Adv. Mater.*, 2022, **34**, 2204681.
20 S. Guo, S. Liang, B. Zhang, G. Fang, D. Ma and J. Zhou, *ACS Nano*, 2019, **13**, 13456–13464.

